A Dual-Coupled *LCC*-Compensated IPT System With a Compact Magnetic Coupler

Fei Lu , *Student Member, IEEE*, Hua Zhang , *Student Member, IEEE*, Heath Hofmann, *Senior Member, IEEE*, Wencong Su, *Member, IEEE*, and Chunting Chris Mi , *Fellow, IEEE*

Abstract—**This paper proposes a dual-coupled *LCC*-compensated inductive power transfer system with a compact magnetic coupler to improve misalignment performance. In the magnetic coupler, the main coils form the first coupling, and compensation inductors are integrated with the main coils to form a second coupling. In the design presented in this paper, the main coils are unipolar and the compensation inductors are in a Double D structure. The fundamental harmonics approximation method is used to analyze the circuit, and the couplings between the main coils and compensation inductors are considered to determine the net power flow. In misalignment cases, it is shown that the coupling between the compensation inductors, and the cross couplings between the compensation inductors and main coils, contribute to increasing the system power. A 3.5 kW prototype is designed and implemented to validate the proposed dual-coupled system. The primary coil size is 450 mm × 450 mm, and the secondary coil size is 300 mm × 300 mm. Experimental results show that the proposed dual-coupled system can significantly improve the misalignment performance, and retains at least 56.8% and 82.6% of the well-aligned power at 150 mm misalignment in the *x*- and *y*-directions, respectively.**

Index Terms—**Dual coupling, inductive power transfer, *LCC* compensation, misalignment improvement, power flow analysis.**

I. INTRODUCTION

INDUCTIVE power transfer (IPT) technology is an effective method to charge electric vehicles [1], [2]. It usually consists of two planar coils, forming a loosely coupled transformer, and the compensation circuitry [3], [4]. The ac–dc efficiency of an IPT system from the power grid to the battery has reached 93% [5], which is comparable to a conductive charger.

The performance of an IPT system is determined by the compensation topologies, which can be clarified as series–series

(SS) [6], [7], series–parallel [8], parallel–series [9], parallel–parallel [10], and *LCC* circuits [11], [12]. The SS compensation circuit has been widely used in electric vehicle charging applications because of its simplicity. However, its output power is inversely proportional to the coils' coupling coefficient, and so the primary current increases rapidly when a receiver is not present. In comparison, the *LCC* compensation circuit provides power in proportion to the coupling coefficient, and achieves a constant-current operating mode for battery charging applications [13], [14]. However, the *LCC* circuit requires more components, which increases the system complexity.

In an *LCC*-compensated IPT system, there are three options when designing compensation inductors: air-core inductor [13], annular-core inductor [15], and integrated inductor [16]. In the air- and annular-core design, the inductors and main coils are separated, and the only coupling in the system is between the main coils, which can be denoted as a single-coupled IPT system. In an integrated design, the compensation inductors are integrated into the main coils, and there are both main coupling and compensation coupling, which is denoted as a dual-coupled IPT system. Air-core inductors can eliminate magnetic losses and increase efficiency [13], [17]. However, electromagnetic interference (EMI) is a problem. Annular-core inductors have the advantage of confining magnetic fields inside the ferrite core and alleviating the EMI. However, extra space is required for these external inductors. Therefore, integrated inductors can help reduce the system volume [18].

In previous attempts to integrate compensation inductors with main coils, the couplings with compensation inductors were not taken into account [19]–[21]. For example, the size of compensation inductors is usually much smaller than the main coils [19]–[21], and the couplings induced by the compensation inductors are relatively small or even negligible. In this work, the size of the compensation inductors is the same as those of the main coils. The couplings with the compensation inductors become comparable to the main coupling. It will be shown in this paper that this coupling can be used to increase power transfer and improve the misalignment performance.

In previous research, the misalignment problem in an IPT system has been studied, and two effective solutions has been proposed. The first solution is from the system design point of view, in which the structure of the inductive coupler is designed to achieve a good misalignment performance. For example, the unipolar structure [22], double D (DD) structure [23], [24], and DDQ structure [25], [26] have been proposed. However,

Fig. 1.   Structure and dimensions of the integrated magnetic coupler. (a) 3-D view. (b) Front view.

TABLE I
PARAMETERS DESCRIBING THE INTEGRATED COUPLER

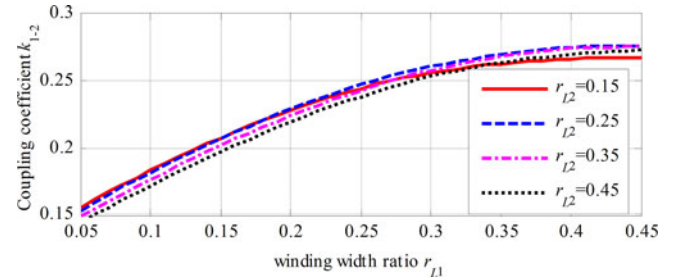| Parameter	Description	Parameter	Description
l_1	Transmitter length	l_2	Receiver length
l_{w1}	Winding width of L_1	l_{w2}	Winding width of L_2
l_{wf1}	Winding width of L_{f1}	l_{wf2}	Winding width of L_{f2}
d_a	Air-gap distance	d_{A1}	Ferrite–aluminum distance

Fig. 2.   Maxwell-simulated k_{1-2} with different width ratio r_{L1} and r_{L2}.

since the coupling coefficient is mainly determined by the size, the variation of structure does not significantly improve the misalignment performance. Also, an additional coupler can be used [27]. In the second solution, additional dc–dc converters are used at the primary and secondary sides to regulate power in misalignment cases. For example, Bosshard and Kolar [28] propose a method to use dc–dc converters to adjust its power and efficiency. Compared to the previous research, the contribution of this work is that misalignment performance is significantly improved without increasing coupler size or adding dc–dc converters.

II. INTEGRATED MAGNETIC COUPLER DESIGN

A. Coupler Structure

Fig. 1(a) shows the three-dimensional (3-D) view of the integrated magnetic coupler, in which L_1, L_2 are the main coils and L_{f1}, L_{f2} are the compensation inductors. Mutual inductances are defined as

$$M_{1-2} = k_{1-2} \cdot \sqrt{L_1 L_2}, M_{f1-f2} = k_{f1-f2} \cdot \sqrt{L_{f1} L_{f2}}$$

$$M_{1-f1} = k_{1-f1} \cdot \sqrt{L_1 L_{f1}}, M_{2-f2} = k_{2-f2} \cdot \sqrt{L_2 L_{f2}}$$

$$M_{1-f2} = k_{1-f2} \cdot \sqrt{L_1 L_{f2}}, M_{f1-2} = k_{f1-2} \cdot \sqrt{L_{f1} L_2} \quad (1)$$

where k_{1-2}, k_{1-f1}, k_{1-f2}, k_{2-f1}, k_{1-f2}, and k_{f1-f2} are the coupling coefficient in the magnetic coupler.

It should be noted that only the different-side coupling coefficients, i.e., k_{1-2}, k_{1-f2}, k_{f1-f2}, and k_{f1-2}, can contribute to

power transfer. Therefore, the size of compensation inductors is designed to be the same as the main coils to maximize coupling.

Meanwhile, the same-side coupling coefficients, k_{1-f1} and k_{2-f2}, do not contribute to transfer power. In this design, main coils are unipolar and the compensation inductors are in DD structure to minimize k_{1-f1} and k_{2-f2}. It needs to be clarified that, as an alternative design, the main coils can also be in DD structure while the compensation inductors are unipolar.

Fig. 1(b) shows the front view of the integrated magnetic coupler. Ferrite plates are 25 mm larger than the coils. Also, aluminum sheets are 25 mm larger than the ferrite plates. The distance d_{A1} between the ferrite and aluminum plates is 15 mm in order to reduce induced eddy-current losses in the shielding.

The parameters describing the coupler dimensions are defined in Table I. Both the transmitter and receiver are square, and their lengths are defined as l_1 and l_2, respectively.

B. Dimension Design

The dimensions of the coils are chosen according to the recommendations in SAE J2954 standard [29]. The primary coil size is $l_1 = 450$ mm, and the secondary coil size is $l_2 = 300$ mm. The transfer distance is $d_a = 120$ mm. To simplify the design process, winding width ratios are defined

$$r_{L1} = \frac{l_{w1}}{l_1}, r_{Lf1} = \frac{2 \times l_{wf1}}{l_1}, r_{L2} = \frac{l_{w2}}{l_2}, r_{Lf2} = \frac{2 \times l_{wf2}}{l_2}. \quad (2)$$

It needs to be emphasized that, for a practical coil, the range of winding ratios is usually from 0.05 to 0.45. Finite element analysis by Maxwell is used in simulation.

Fig. 2 shows that, in the well-aligned case, the primary coil width ratio r_{L1} dominates the main coupling k_{1-2}, and the influence of r_{L2} can be neglected. Therefore, the primary winding width ratio r_{L1} is chosen to be 0.45.

In x-direction misalignment, k_{1-2} is simulated in Fig. 3, in which r_{L1} is 0.45 and r_{L2} varies. For the main coils, the misalignment performances are the same in the x- and y-directions,
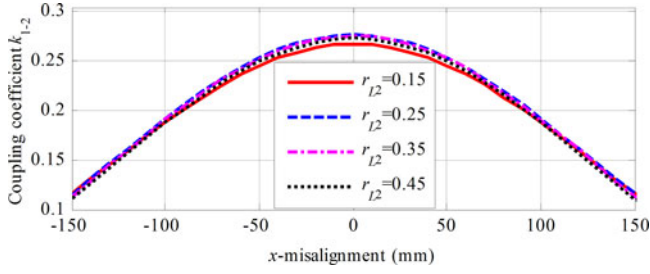
Fig. 3. Maxwell-simulated k_{1-2} in x-misalignment when $r_{L1} = 0.45$ and r_{L2} varies.
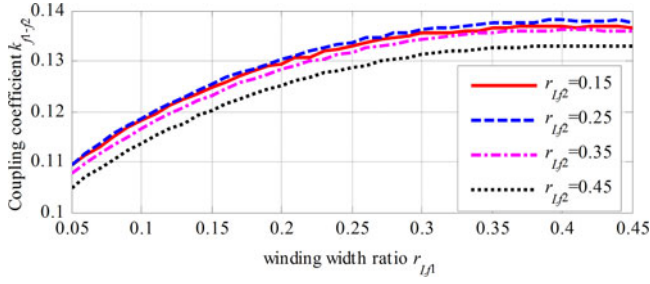

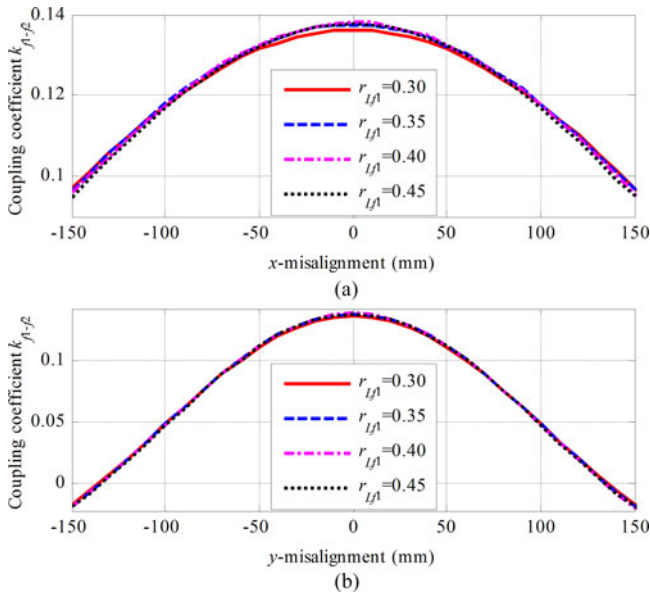Fig. 4. Maxwell-simulated k_{f1-f2} with different r_{L1} and r_{L2} at well aligned.

Fig. 5. Maxwell-simulated k_{f1-f2} in misalignment when $r_{Lf2} = 0.25$ and r_{Lf1} varies. (a) x-misalignment. (b) y-misalignment.

because they are unipolar and square. In this design, r_{L2} is therefore set to 0.45 to reduce conduction losses. Then, k_{1-2} is therefore 0.270 in the well-aligned case, and decreases to 0.110 at 150 mm misalignment.

For the compensation inductors, the simulated k_{f1-f2} is in Fig. 4. It indicates that k_{f1-f2} increases with the increasing r_{Lf1}, and it is almost constant after r_{Lf1} is 0.30. Furthermore, k_{f1-f2} is largest when $r_{Lf2} = 0.25$. Therefore, the optimal range of r_{Lf1} is from 0.30 to 0.45, and r_{Lf2} is set to 0.25.

The x- and y-direction misalignment performance of k_{f1-f2} is shown in Fig. 5. It is set to 0.30 to reduce the usage of Litz
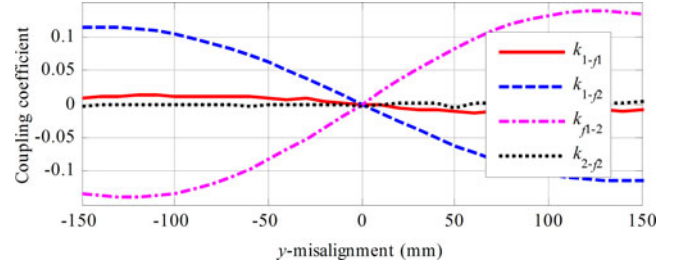

Fig. 6. Maxwell-simulated k_{1-f1}, k_{1-f2}, k_{f1-2}, and k_{1-f2} in y-misalignment cases when $r_{L1} = 0.45$, $r_{L2} = 0.45$, $r_{Lf1} = 0.30$, and $r_{Lf2} = 0.25$.
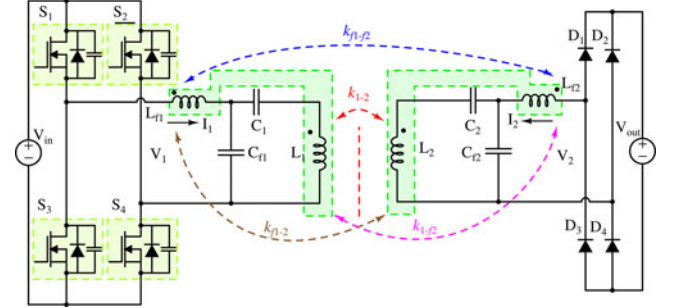

Fig. 7. Circuit topology of an *LCC*-compensated dual-coupled IPT system.

wire. When $r_{Lf1} = 0.30$ and $r_{Lf2} = 0.25$, $k_{f1-f2} = 0.136$ in the well-aligned case, is 0.097 at 150 mm x-misalignment, and is –0.017 at 150 mm y-misalignment.

The couplings coefficient k_{1-f1}, k_{1-f2}, k_{f1-2}, and k_{2-f2} need to be considered in y-misalignment cases due to the asymmetry of the coupler structure, as shown in Fig. 6. The maximum k_{1-f1} is 0.015 and the maximum k_{2-f2} is 0.005, which can be both neglected. However, the maximum cross couplings k_{1-f2} and k_{f1-2} are 0.115 and 0.139, and so should be considered.

III. WORKING PRINCIPLE OF *LCC*-COMPENSATED DUAL-COUPLED IPT SYSTEM

A. Coupler Structure

The circuit topology of an *LCC*-compensated dual-coupled IPT system is shown in Fig. 7. Coils L_1 and L_{f1} are integrated together as a transmitter. Coils L_2 and L_{f2} are integrated as a receiver. There are four significant couplings, k_{1-2}, k_{f1-f2}, k_{1-2}, and k_{f1-2} in the system. The compensation inductors share the same ferrite and shielding plates with the main coils.

In the compensation circuit, capacitors C_1 and C_{f1} are used to resonate with L_1 and L_{f1}, respectively, and C_2 and C_{f2} resonate with L_2 and L_{f2}. At the primary side, a dc voltage source V_{in} is used as the power supply, followed by a full-bridge inverter used. Furthermore, an uncontrolled diode rectifier is adopted at the secondary side to provide dc current to a battery load V_{out}.

B. Output Power Calculation

The fundamental harmonics approximation (FHA) method is used, as shown in Fig. 8. The square-wave voltages can be approximated as sinusoidal sources. The magnetic couplings
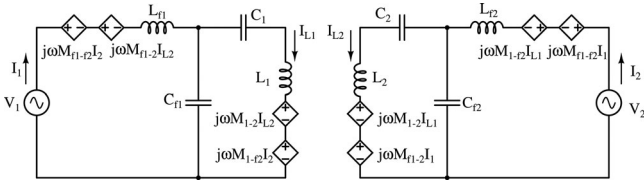
Fig. 8.   Fundamental harmonics approximation of the circuit.

are represented by dependent sources. The power losses of the components are neglected to simplify the analysis.

The KCL equations of Fig. 8 are expressed as in (3), shown at the bottom of this page.

The resonant relationship is expressed as

$$\omega^2 L_{f1} C_{f1} = \omega^2 L_{f2} C_{f2} = 1$$
$$\omega^2 (L_1 - L_{f1}) C_1 = \omega^2 (L_2 - L_{f2}) C_2 = 1. \tag{4}$$

By substituting (4) into (3), it can be simplified as

$$
\begin{bmatrix}
0 & j\omega L_{f1} & j\omega M_{f1-f2} & j\omega M_{f1-2} \\
j\omega L_{f1} & 0 & j\omega M_{1-f2} & j\omega M_{1-2} \\
j\omega M_{f1-f2} & j\omega M_{1-f2} & 0 & j\omega L_{f2} \\
j\omega M_{f1-2} & j\omega M_{1-2} & j\omega L_{f2} & 0
\end{bmatrix}
$$
$$
\cdot
\begin{bmatrix}
I_1 \\
I_{L1} \\
I_2 \\
I_{L2}
\end{bmatrix}
=
\begin{bmatrix}
V_1 \\
0 \\
V_2 \\
0
\end{bmatrix}. \tag{5}
$$

Therefore, the input and output current can be calculated as

$$
\begin{bmatrix}
I_1 \\
I_2
\end{bmatrix}
=
\begin{bmatrix}
\frac{-c \cdot M_{1-2}}{b^2 - a \cdot c} & \frac{b \cdot M_{1-2}}{b^2 - a \cdot c} \\
\frac{b \cdot M_{1-2}}{b^2 - a \cdot c} & \frac{-a \cdot M_{1-2}}{b^2 - a \cdot c}
\end{bmatrix}
\cdot
\begin{bmatrix}
V_1 \\
V_2
\end{bmatrix} \tag{6}
$$

where, a, b, and c are defined as

$$a = j\omega \cdot (-2M_{f1-2} L_{f1})$$
$$b = j\omega \cdot (-L_{f1} L_{f2} + M_{f1-f2} M_{1-2} - M_{f1-2} M_{1-f2})$$
$$c = j\omega \cdot (-2M_{1-f2} L_{f2}). \tag{7}$$

If V_2 is set as the reference phasor, and the phase difference with V_1 is defined as α, the currents are

$$I_1 = \frac{M_{1-2}}{b^2 - a \cdot c} \cdot [(-c \cdot \cos \alpha \cdot |V_1| + b \cdot |V_2|) - j \cdot c \cdot \sin \alpha \cdot |V_1|]$$

$$I_2 = \frac{M_{1-2}}{b^2 - a \cdot c} \cdot [(b \cdot \cos \alpha \cdot |V_1| - a \cdot |V_2|) + j \cdot b \cdot \sin \alpha \cdot |V_1|]. \tag{8}$$

At the output side, the voltage V_2 is in phase with current $(-I_2)$ [13], which means $(-I_2)$ is a positive real number, resulting in

$$\cos \alpha = \frac{a}{b} \cdot \frac{|V_2|}{|V_1|}. \tag{9}$$

Therefore, the currents are further simplified as

$$I_1 = \frac{M_{1-2}}{b^2 - a \cdot c} \cdot \left(\frac{b^2 - a \cdot c}{b} \cdot |V_2| - j \cdot c \cdot \sin \alpha \cdot |V_1| \right)$$

$$I_2 = \frac{M_{1-2}}{b^2 - a \cdot c} \cdot b \cdot j \cdot \sin \alpha \cdot |V_1|. \tag{10}$$

The output current I_2 only depends on the input voltage V_1, which means the proposed circuit behaves as a current source.

If the main coupling is designed to satisfy $k_{1-2} > 0$, the second equation of (10) indicates $\sin \alpha > 0$, therefore

$$\sin \alpha = \sqrt{1 - \frac{|a|^2}{|b|^2} \cdot \frac{|V_2|^2}{|V_1|^2}}. \tag{11}$$

The system output power is therefore expressed as

$$P_{\text{out}} = |V_2| \cdot |I_2| = M_{1-2} \cdot \frac{|b|}{|b^2 - a \cdot c|} \cdot \sqrt{1 - \frac{|a|^2}{|b|^2} \cdot \frac{|V_2|^2}{|V_1|^2}}$$
$$\cdot |V_1| \cdot |V_2|. \tag{12}$$

If $|V_1| = |V_2|$, the output power can be simplified as

$$P_{\text{out}} = |V_2| \cdot |I_2| = M_{1-2} \cdot \frac{\sqrt{|b|^2 - |a|^2}}{|b^2 - a \cdot c|} \cdot |V_1|^2. \tag{13}$$

By substituting (7) into (13), it is expressed as (14), shown at the bottom of this page.

Using the coupling coefficients in (1), it is simplified as (15), shown at the bottom of next page. where β and γ are defined

$$
\begin{bmatrix}
j\omega L_{f1} + \frac{1}{j\omega C_{f1}} & -\frac{1}{j\omega C_{f1}} & j\omega M_{f1-f2} & j\omega M_{f1-2} \\
-\frac{1}{j\omega C_{f1}} & \frac{1}{j\omega C_1} + \frac{1}{j\omega C_{f1}} + j\omega L_1 & j\omega M_{1-f2} & j\omega M_{1-2} \\
j\omega M_{f1-f2} & j\omega M_{1-f2} & j\omega L_{f2} + \frac{1}{j\omega C_{f2}} & -\frac{1}{j\omega C_{f2}} \\
j\omega M_{f1-2} & j\omega M_{1-2} & \frac{1}{j\omega C_{f2}} & \frac{1}{j\omega C_2} + \frac{1}{j\omega C_{f2}} + j\omega L_2
\end{bmatrix}
\cdot
\begin{bmatrix}
I_1 \\
I_{L1} \\
I_2 \\
I_{L2}
\end{bmatrix}
=
\begin{bmatrix}
V_1 \\
0 \\
V_2 \\
0
\end{bmatrix} \tag{3}
$$

$$P_{\text{out}} = \frac{M_{1-2} \cdot \sqrt{(L_{f1} L_{f2} - M_{1-2} M_{f1-f2} + M_{f1-2} M_{1-f2})^2 - 4(M_{f1-2} L_{f1})^2}}{\omega \left| (L_{f1} L_{f2} - M_{1-2} M_{f1-f2} + M_{f1-2} M_{1-f2})^2 - 4(M_{f1-2} L_{f1})(M_{1-f2} L_{f2}) \right|} \cdot |V_1|^2 \tag{14}$$

as follows:

$$\beta = \frac{\sqrt{L_1 L_2}}{\sqrt{L_{f1} L_{f2}}}, \gamma = \frac{L_{f1}}{L_{f2}} \cdot \frac{\sqrt{L_{f1} L_2}}{\sqrt{L_{f2} L_1}}. \tag{16}$$

Three parameters K_1, K_2, and K_3 can be defined as

$$K_1 = k_{1-2} k_{f1-f2} \beta, K_2 = k_{f1-2} k_{1-f2} \beta, K_3 = k_{f1-2} k_{f1-2} \beta. \tag{17}$$

It shows that K_1, K_2, and K_3 relate to the coupling coefficient and inductance ratio. The output power is simplified as

$$P_{\text{out}} = \frac{k_{1-2} \sqrt{L_1 L_2}}{\omega L_{f1} L_{f2}} \cdot \frac{\sqrt{(1 - K_1 + K_2)^2 - 4K_3 \gamma}}{\left| (1 - K_1 + K_2)^2 - 4K_2 \right|} \cdot |V_1|^2. \tag{18}$$

If the parameters satisfy $|K_1 K_2| << 1.0$, $|K_1 K_3| << 1.0$, and $|K_2 K_3| << 1.0$, the output power can be approximated to be

$$P_{\text{out}} \approx \frac{k_{1-2} \sqrt{L_1 L_2}}{\omega L_{f1} L_{f2}} \cdot \frac{1 - K_1 + K_2 - 2K_3 \gamma}{1 - 2K_1 - 2K_2} \cdot |V_1|^2. \tag{19}$$

Furthermore, it can be simplified as

$$P_{\text{out}} \approx \frac{k_{1-2} \sqrt{L_1 L_2}}{\omega L_{f1} L_{f2}} \cdot \frac{1}{1 - K_1 - 3K_2 + 2K_3 \gamma} \cdot |V_1|^2. \tag{20}$$

According to the coupler design in Section II, there is $k_{f1-2} \approx k_{1-f2}$, resulting in $K_2 \approx K_3$ and the system power is

$$P_{\text{out}} \approx \frac{k_{1-2} \sqrt{L_1 L_2}}{\omega L_{f1} L_{f2}} \cdot \frac{1}{1 - K_1 - (3 - 2\gamma) K_2} \cdot |V_1|^2. \tag{21}$$

When well aligned, there are no cross couplings k_{f1-2} and k_{1-f2}, which means $K_2 = K_3 = 0$. The output power is simplified as

$$P_{\text{out}} = \frac{\sqrt{L_1 L_2}}{\omega L_{f1} L_{f2}} \cdot \frac{k_{1-2}}{1 - K_1} \cdot |V_1|^2. \tag{22}$$

In an IPT system, misalignment leads to a decrease of k_{1-2}. According to (20), the system power also drops with k_{1-2}. Since K_1, K_2, and K_3 relate to the magnetic couplings, they can be designed to improve the misalignment performance.

C. Power Flow Analysis

It is also necessary to analyze the power flow among the magnetic couplings, which can be expressed as

$$S_{f1-f2} = P_{f1-f2} + jQ_{f1-f2} = j\omega M_{f1-f2} \cdot I_1 \cdot I_2^*$$

$$S_{1-f2} = P_{1-f2} + jQ_{1-f2} = j\omega M_{1-f2} \cdot I_{L1} \cdot I_2^*$$

$$= j\omega \frac{M_{1-f2}}{M_{1-2}} \cdot (-M_{f1-2} \cdot I_1 - L_{f2} \cdot I_2) \cdot I_2^*$$

$$S_{f1-2} = P_{f1-2} + jQ_{f1-2} = j\omega M_{f1-2} \cdot I_1 \cdot I_{L2}^*$$

$$= j\omega \frac{M_{f1-2}}{M_{1-2}} \cdot I_1 \cdot (-L_{f1} \cdot I_1 - M_{1-f2} \cdot I_2)^*$$

$$S_{1-2} = P_{1-2} + jQ_{1-2} = j\omega M_{1-2} \cdot I_{L1} \cdot I_{L2}^*$$

$$= \frac{j\omega}{M_{1-2}} (-M_{f1-2} \cdot I_1 - L_{f2} \cdot I_2)$$

$$\cdot (-L_{f1} \cdot I_1 - M_{1-f2} \cdot I_2)^*. \tag{23}$$

If the phase difference between I_1 and $(-I_2)$ is defined as α_I, according to (9) and (10), there is

$$\tan \alpha_I = -\frac{b^2 - a \cdot c}{a \cdot c} \cdot \frac{\cos \alpha}{\sin \alpha}. \tag{24}$$

It is further calculated that

$$I_1 \cdot I_2^* = I_1 \cdot I_2 = \left(\frac{M_{1-2}}{b} \cdot |V_2| - M_{1-2} \cdot \frac{j \cdot c \cdot \sin \alpha \cdot |V_1|}{b^2 - a \cdot c} \right)$$

$$\cdot I_2 = -\frac{M_{1-2}}{b} \cdot P_{\text{out}} + j \cdot \frac{M_{1-2}}{b} \cdot \frac{1}{\tan \alpha_I} \cdot P_{\text{out}}$$

$$I_1 \cdot I_1^* = j \cdot \frac{M_{1-2}}{b} \cdot \frac{1}{\sin \alpha_I} \cdot |V_2| \cdot M_{1-2} \cdot \frac{j \cdot c \cdot \sin \alpha}{b^2 - a \cdot c} \frac{1}{\cos \alpha_I}$$

$$\cdot |V_1| = -j \cdot \frac{M_{1-2} \cdot c}{b^2} \cdot \frac{1}{\sin \alpha_I \cos \alpha_I} \cdot P_{\text{out}}$$

$$I_2 \cdot I_2^* = M_{1-2} \cdot \frac{j \cdot b \cdot \sin \alpha}{b^2 - a \cdot c} \cdot |V_1| \cdot I_2$$

$$= -j \cdot \frac{M_{1-2}}{c} \cdot \frac{1}{\tan \alpha_I} \cdot P_{\text{out}}. \tag{25}$$

By substituting (25) into (23), the complex power received at the secondary side is expressed in (26).

Using the parameter definitions, the complex power received at the secondary side is simplified in Table II. There are both active and reactive power transfers among the couplings.

The active power flow across the couplings is shown in Fig. 9. If the power losses in the circuit components are neglected, the total power transferred from the primary side is equal to the total power received at the secondary side. This shows that active power is transferred from the primary side to the secondary side through four paths. The first path is from the primary main coil

$$P_{\text{out}} = \frac{k_{1-2} \sqrt{L_1 L_2}}{\omega L_{f1} L_{f2}} \cdot \frac{\sqrt{(1 - k_{1-2} k_{f1-f2} \beta + k_{f1-2} k_{1-f2} \beta)^2 - 4k_{f1-2} k_{f1-2} \beta \gamma}}{\left| (1 - k_{1-2} k_{f1-f2} \beta + k_{f1-2} k_{1-f2} \beta)^2 - 4k_{f1-2} k_{1-f2} \beta \right|} \cdot |V_1|^2 \tag{15}$$

TABLE II
POWER RECEIVED AT SECONDARY SIDE THROUGH MAGNETIC COUPLINGS

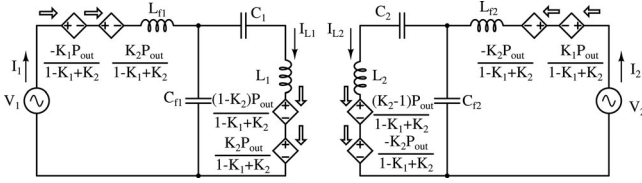| Coupling	Active power	Reactive power
$L_{f1} - L_{f2}$	$P_{f1-f2} = \frac{K_1 \cdot P_{\text{out}}}{1-K_1+K_2}$	$Q_{f1-f2} = \frac{-K_1}{1-K_1+K_2} \cdot \frac{1}{\tan \alpha_I} P_{\text{out}}$
$L_1 - L_{f2}$	$P_{1-f2} = \frac{-K_2 \cdot P_{\text{out}}}{1-K_1+K_2}$	$Q_{1-f2} = \frac{K_2}{1-K_1+K_2} \cdot \frac{1}{\tan \alpha_I} P_{\text{out}} + \frac{1}{2} \cdot \frac{1}{\tan \alpha_I} P_{\text{out}}$
$L_{f1} - L_2$	$P_{f1-2} = \frac{-K_2 \cdot P_{\text{out}}}{1-K_1+K_2}$	$Q_{f1-2} = \frac{K_2}{1-K_1+K_2} \cdot \frac{1}{\tan \alpha_I} P_{\text{out}} + \frac{-2K_2}{(1-K_1+K_2)^2 \sin \alpha_I \cdot \cos \alpha_I} P_{\text{out}}$
$L_1 - L_2$	$P_{1-2} = \frac{-(1-K_2) \cdot P_{\text{out}}}{1-K_1+K_2}$	$Q_{1-2} = \frac{1-K_2}{1-K_1+K_2} \cdot \frac{1}{\tan \alpha_I} P_{\text{out}} + \frac{-1}{2} \cdot \frac{1}{\tan \alpha_I} P_{\text{out}} + \frac{2K_2}{(1-K_1+K_2)^2 \sin \alpha_I \cdot \cos \alpha_I} \cdot P_{\text{out}}$

Fig. 9. Active power flow across the couplings in a dual-coupled system.

L_1 to the secondary main coil L_2, the second path is from the primary main coil L_1 to the secondary compensation inductor L_{f2}, the third path is from the primary compensation inductor L_{f1} to the secondary main coil L_2, and the fourth path is from the primary compensation inductor L_{f1} to the secondary compensation inductor L_{f2}. These paths can be exploited to improve the misalignment performance

$$S_{f1-f2} = P_{f1-f2} + jQ_{f1-f2} = \left(\frac{-j\omega M_{1-2} M_{f1-f2}}{b} \cdot P_{\text{out}} \right)$$

$$+ \left(\frac{-\omega M_{1-2} M_{f1-f2}}{b} \cdot \frac{1}{\tan \alpha_I} P_{\text{out}} \right) \quad S_{1-f2} = P_{1-f2}$$

$$+ jQ_{1-f2} = \left(\frac{j\omega M_{1-f2} M_{f1-2}}{b} \cdot P_{\text{out}} \right) + \left(\frac{\omega M_{1-f2} M_{f1-2}}{b} \right.$$

$$\cdot \frac{1}{\tan \alpha_I} \cdot P_{\text{out}} + \frac{\omega M_{1-f2} L_{f2}}{c} \cdot \frac{1}{\tan \alpha_I} \left. P_{\text{out}} \right) S_{f1-2} = P_{f1-2}$$

$$+ jQ_{f1-2} = \left(\frac{j\omega M_{1-f2} M_{f1-2}}{b} \cdot P_{\text{out}} \right) + \left(\frac{\omega M_{1-f2} M_{f1-2}}{b} \right.$$

$$\cdot \frac{1}{\tan \alpha_I} \cdot P_{\text{out}} + \frac{-\omega M_{f1-2} \cdot L_{f1} \cdot c}{b^2 \cdot \sin \alpha_I \cdot \cos \alpha_I} \cdot P_{\text{out}} \left. \right) S_{1-2} = P_{1-2}$$

$$+ jQ_{1-2} = \left(\frac{j\omega L_{f1} L_{f2}}{b} \cdot P_{\text{out}} + \frac{-j\omega M_{1-f2} M_{f1-2}}{b} \cdot P_{\text{out}} \right)$$

$$+ \left(\frac{-\omega M_{1-f2} M_{f1-2}}{b} \cdot \frac{1}{\tan \alpha_I} P_{\text{out}} + \frac{-\omega M_{1-f2} L_{f2}}{c} \right.$$

$$\cdot \frac{1}{\tan \alpha_I} P_{\text{out}} + \frac{\omega M_{f1-2} \cdot L_{f1} \cdot c}{b^2 \cdot \sin \alpha_I \cdot \cos \alpha_I} \cdot P_{\text{out}} + \frac{-\omega L_{f1} L_{f2}}{b}$$

$$\cdot \frac{1}{\tan \alpha_I} \cdot P_{\text{out}} \left. \right). \tag{26}$$

IV. EXAMPLE OF *LCC*-COMPENSATED DUAL-COUPLED IPT SYSTEM

A. Misalignment Performance Analysis

The conventional *LCC*-compensated system [13], in which the coupler contains only the main coils, is defined as a single-coupled system. In this paper, the proposed system, in which the coupler contains the main coils and the compensation inductors, is defined as a dual-coupled system. Their output power are denoted as P_{single} and P_{dual}, and expressed as

$$\begin{cases} P_{\text{single}} = \frac{\sqrt{L_1 L_2}}{\omega L_{f1} L_{f2}} \cdot k_{1-2} \cdot |V_1|^2 \\ P_{\text{dual}} = \frac{k_{1-2}\sqrt{L_1 L_2}}{\omega L_{f1} L_{f2}} \cdot \frac{1}{1-K_1-(3-2\gamma)K_2} \cdot |V_1|^2 \end{cases}. \tag{27}$$

When there is misalignment, k_{1-2} decreases, which leads to a decrease of system power. According to the definitions of K_1 and K_2, the structure of the proposed coupler can be designed to achieve increasing K_1 and K_2 with increasing misalignment. In this way, the misalignment performance is improved.

Considering the simulation in Section II, the polarity of L_{f2} should be flipped to achieve $k_{f1-f2} < 0$ and $k_{f1-2}k_{1-f2} > 0$, which leads to the increasing of K_1 and K_2 with misalignment. Using (20) and (22), a coefficient h can be defined as

$$h = \frac{(1-K_1)|_{\text{well-aligned}}}{(1-K_1-3K_2+2K_3\gamma)|_{\text{mis-aligned}}}. \tag{28}$$

According to (17) and the parameters in Section II, h can be calculated in 150 mm *x*- and *y*-misalignment cases as

$$\begin{cases} h|_{x=150 \text{ mm}} = \frac{1+0.0367\beta}{1+0.0107\beta} \\ h|_{y=150 \text{ mm}} = \frac{1+0.0367\beta}{1-(0.0499-0.0386\gamma)\beta} \end{cases}. \tag{29}$$

It shows that increasing β helps to increase h in both *x*- and *y*-misalignment, which can improve the misalignment performance. Also, decreasing γ improves the *y*-misalignment performance.

In *x*- and *y*-misalignment, the normalized output power relationship with the inductance ratios β and γ is shown in Fig. 10. It is compared to a single-coupled IPT system using only the main coupling coefficient k_{1-2}.

There are two comparisons in Fig. 10. First, a single-coupled system is compared to the proposed dual-coupled system. The proposed system improves misalignment performance. Second, different dual-coupled systems have different performances. It validates that increasing β and decreasing γ both improve the
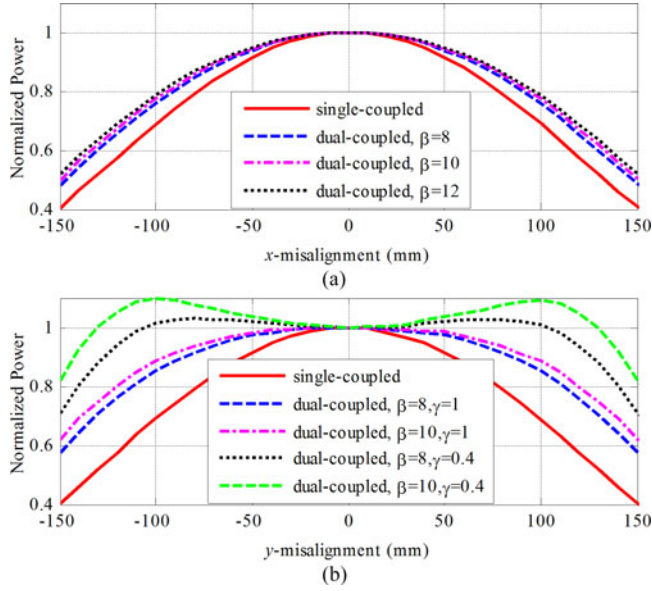
Fig. 10. Comparison of a single-coupled and dual-coupled *LCC*-compensated IPT systems with different inductance ratios β and γ (a) Calculated normalized output power in *x*-misalignment. (b) Calculated normalized output power in *y*-misalignment.

misalignment performance. Fig. 10 and (29) provide guidelines to design the circuit parameters.

Fig. 10(a) shows the *x*-direction misalignment. Since cross couplings k_{1-f2} and k_{f1-2} are small, the *x*-direction misalignment performance is only determined by β and is independent of γ. The *x*-direction misalignment is improved with increasing β.

Fig. 10(b) shows the *y*-direction misalignment, in which the output power increases with increasing β and decreasing γ. When β becomes larger, there are two peaks in the output power, which can increase the component voltage stress.

B. Circuit Parameter Design

In this section, a 3.5 kW system is designed. According to Fig. 10, the inductance ratios are selected to be $\beta = 8.5$ and $\gamma = 0.4$. Considering the size difference of main coils, the inductances satisfy $L_1 = 1.5 \times L_2$. Therefore, according to (4), (16), and (18), the specifications and circuit parameters are shown in Table III.

The parameters K_1, K_2, and K_3 can be calculated for different *x*- and *y*-direction misalignments, as shown in Fig. 11.

Fig. 11(a) shows K_1 increases with the *x*-direction misalignment. Since k_{1-f2} and k_{f1-2} are zero in the *x*-direction misalignment, K_2 and K_3 are also zero. According to (20), increasing K_1 helps to improve the *x*-direction misalignment performance.

Fig. 11(b) shows K_1 increases with the *y*-direction misalignment. According to (18) and (20), increasing K_1, K_2, and K_3 leads to an improvement of misalignment. Since there is a maximum value of K_2 and K_3, it indicates that there could be a maximum value of power, which is consistent with the two peaks in the waveform of system power in Fig. 10(b).

TABLE III
SYSTEM SPECIFICATIONS AND CIRCUIT PARAMETERS

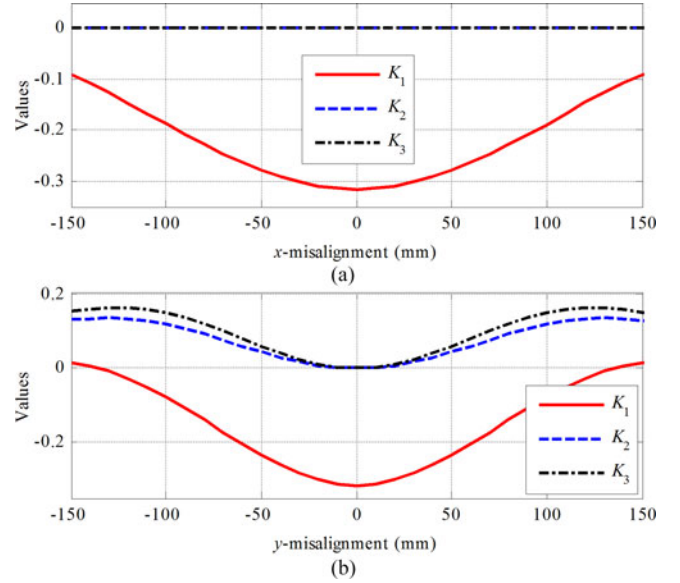| Parameter	Value	Parameter	Value
V_{in}	220 V	V_{out}	220 V
l_1	450 mm	l_2	300 mm
l_{w1}	202 mm	l_{w2}	135 mm
l_{wf1}	67 mm	l_{wf2}	37 mm
d_a	120 mm	f_{sw}	85 kHz
k_{1-2} (well aligned)	0.270	k_{f1-f2} (well aligned)	0.136
k_{1-f2} (maximum)	0.115	k_{f1-2} (maximum)	0.139
L_{f1}	28 μH	L_{f2}	45 μH
L_1	360 μH	L_2	240 μH
C_{f1}	125.2 nF	C_{f2}	77.9 nF
C_1	10.6 nF	C_2	18.0 nF

Fig. 11. Calculated K_1, K_2, and K_3 at *x*- and *y*-direction misalignment (a) *x*-misalignment. (b) *y*-misalignment.

Using Table II and Fig. 11, the power distribution among the couplings is studied as shown in Fig. 12. Compare Figs. 10 and 12, it shows that the the curve of P_{1-2} in Fig. 12 is much smoother than that in Fig. 10, either with *x*- or *y*-misalignment. It is because the integration of the compensation inductors changes the power flow. It is also consistent with the definition of P_{1-2} in Table II, which shows that K_1 and K_2 can contribute to improve the misalignment performance.

Fig. 12(a) indicates that, in *x*-misalignment, P_{1-2} and P_{f1-f2} contribute to the system total power P_{out}. There are two power transfer paths: from L_1 to L_2 and from L_{f1} to L_{f2}.

Fig. 12(b) indicates that, in *y*-misalignment, P_{1-2}, P_{1-f2}, P_{f1-2}, and P_{f1-f2} contribute to the system total power P_{out}. There are four power transfer paths: from L_1 to L_2, from L_1 to L_{f2}, from L_{f1} to L_2, and from L_{f1} to L_{f2}.

C. System Simulation

LTspice is used in simulation. C_2 is increased by 10% to 19.8 nF to realize a soft-switching condition [13]. In the well-aligned case, the waveforms are shown in Fig. 13.
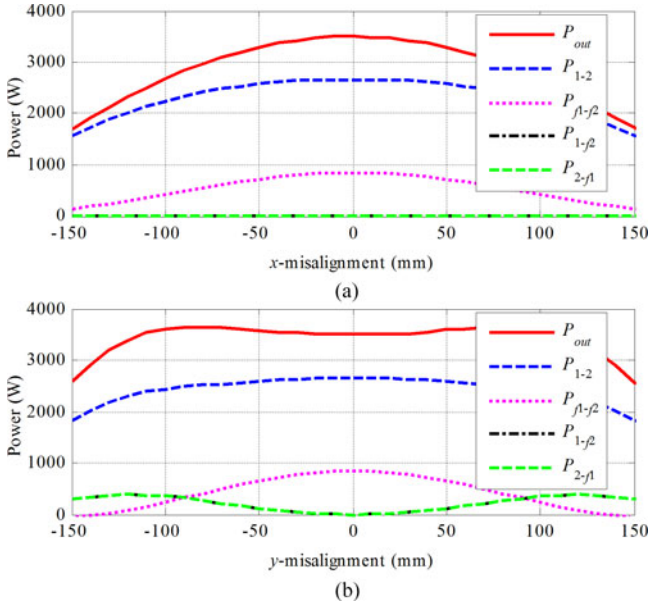
Fig. 12.   Power distribution in the couplings with $\beta = 8.5$ and $\gamma = 0.4$. (a) Calculated power in x-misalignment. (b) Calculated power in y-misalignment.
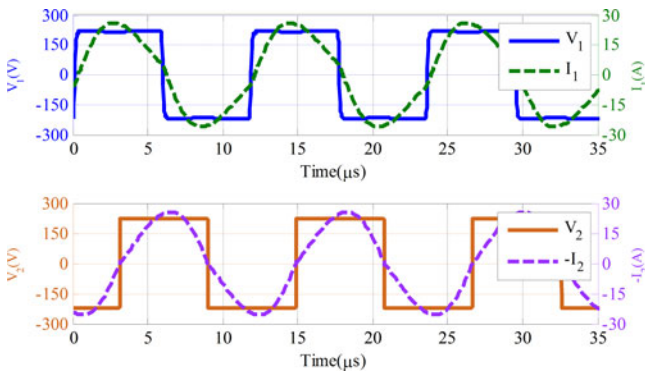

Fig. 13.   LTspice-simulated input and output waveforms at well-aligned case.

Fig. 14.   Maxwell-simulated magnetic field emission of the magnetic coupler. (a) Compact coupler consisting of L_1, L_2, L_{f1}, and L_{f2}. (b) Coupler consisting of L_1 and L_2

It can be seen that, at both the input and output, the voltage and current are almost in phase, which limits the reactive power circulating in the resonant circuit and reduces power losses.

The LTspice simulation provides the currents. According to [13], a 3.5 kW single-coupled system can be designed using the same voltages and dimensions. The number of turns of the coils can be acquired from the prototype design, as shown in Fig. 15 in the next section. The comparison of currents and number of turns is shown in Table IV, which shows that the dual-coupled system can reduce the currents in main coils L_1 and L_2.

Using the currents in Table IV as excitations, magnetic field emissions are simulated in Maxwell, as shown in Fig. 14. According to ICNIRP 2010 guidelines, the limit on magnetic field strength is 27 μT at 85 kHz for general public [30].

In Fig. 14(a), the coupler contains coils L_1, L_2 and inductors L_{f1}, L_{f2}. The safe area is about 200 mm from the side and 300 mm from the top. In Fig. 14(b), the coupler contains only L_1 and L_2, but the excitation currents are larger. The safe area is the same as Fig. 14(a). It can be concluded that the integration of L_{f1} and L_{f2} does not significantly increase field emissions.
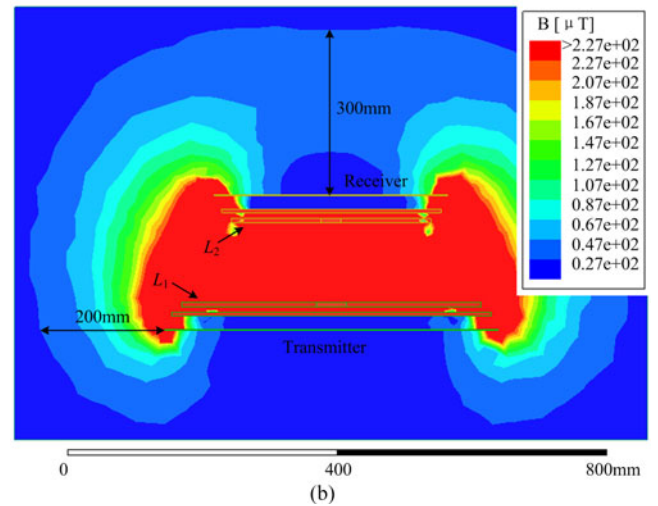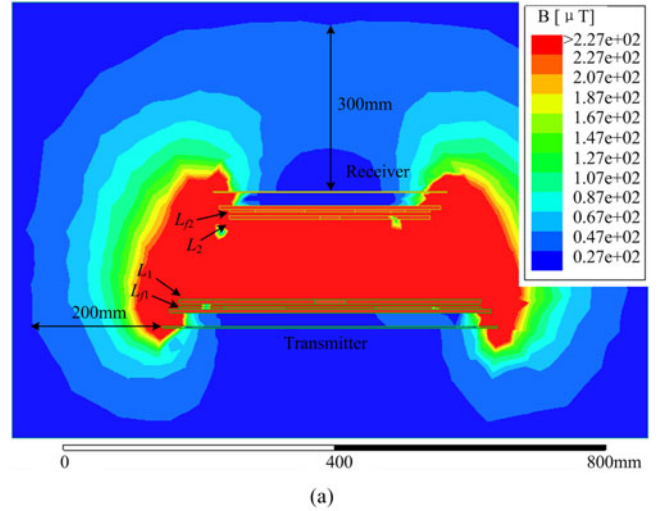
V. EXPERIMENTS

A. Experimental Setup

According to Section II, a prototype of the dual-coupled magnetic coupler is constructed, as shown in Fig. 15.

The coils and inductors are wound by AWG38 Litz wire. To obtain the inductance in Table III, L_1 has 30 turns, L_2 has 31 turns, L_{f1} has 4 turns, and L_{f2} has 6 turns. Multiple litz wire bundles can be connected in parallel to reduce conduction loss. In future research, the IPT system will be studied to optimize the system cost, considering the hardware cost and the saved energy during its life cycle [31]. Using this coupler, an experimental setup is shown in Fig. 16.

In this setup, the magnetic material PC40 is used to build the ferrite plates. They are placed close to the coils to increase the coupling. Aluminum sheets are placed on the top and bottom of the ferrite to provide a shielding effect. To reduce losses, film capacitors with a dissipation factor of 0.05% are chosen. SiC MOSFETs (C2M0025120D) are used in the inverter. A dc
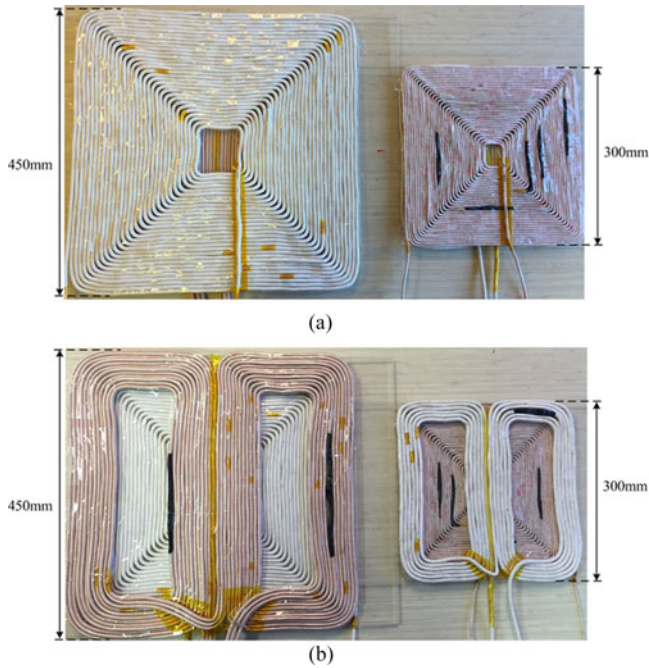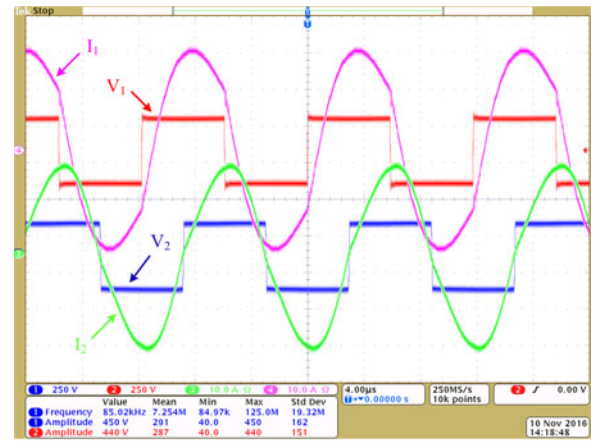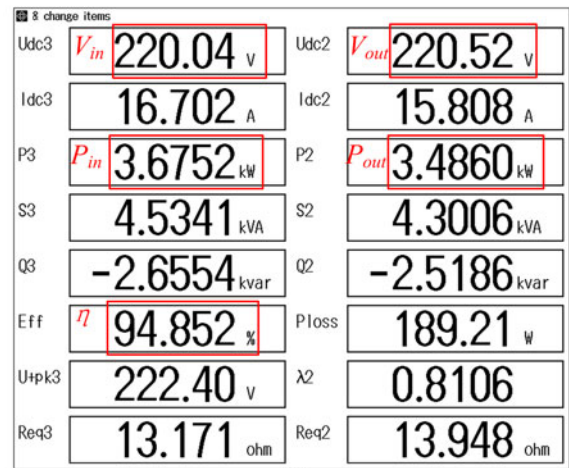
Fig. 15. Prototype of a dual-coupled magnetic coupler. (a) Main coils L_1 and L_2. (b) Compensation inductors L_{f1} and L_{f2}.

TABLE IV
CURRENTS AND NUMBER OF TURNS IN THE SINGLE- AND DUAL-COUPLED
IPT SYSTEMS

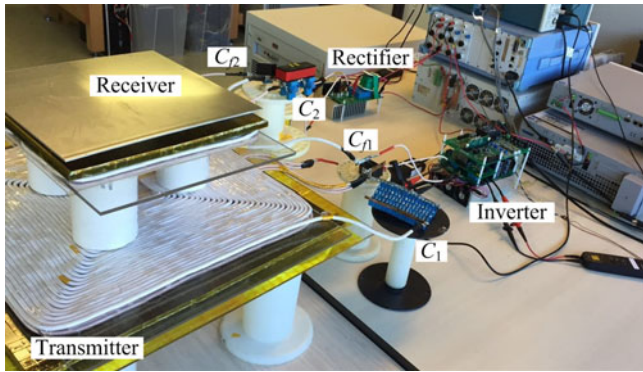| Components	L_{f1}		L_1		L_2		L_{f2}	
Parameters	Current	Turns	Current	Turns	Current	Turns	Current	Turns
Single-coupled	18.3 A	N/A	11.6 A	30	7.5 A	31	17.6 A	N/A
Dual-coupled	18.3 A	4	10.0 A	30	6.3 A	31	17.6 A	6

Fig. 16. Experimental setup of an *LCC*-compensated dual-coupled IPT system.

source is used at the primary side, and the secondary side is connected to an electronic dc load to emulate a battery.

B. Experimental Results

When the transmitter and receiver are well aligned, and the input and output dc voltage are both 220 V, the system reaches full power. The experimental results are shown in Fig. 17.

Fig. 17. Experimental waveforms and efficiency at well-aligned case. (a) Input and output waveforms. (b) Power and efficiency.
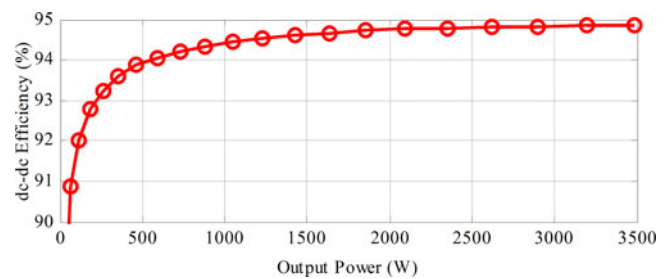
Fig. 18. Experimental results of output power and dc–dc efficiency.

The experimental waveforms agree with Fig. 13, and the soft-switching condition is achieved in the MOSFETs. Therefore, switching losses in the system are small. Fig. 17(b) shows that the system output power can reach 3.48 kW with a dc–dc efficiency of 94.8% from the dc input to the dc output.

In the well-aligned case, the power and efficiency are shown in Fig. 18. The dc–dc efficiency increases with system power. When the power is higher than 500 W, it can achieve a dc–dc efficiency higher than 94%. In future research, better ferrite material will be used to to increase the system efficiency.

Fig. 19. Experimental waveforms in 150 mm x- and y-misalignment cases. (a) x-misalignment. (b) y-misalignment.

Fig. 20. Comparison of experimental and calculated output power. (a) Output power in x-misalignment cases. (b) Output power in y-misalignment cases.

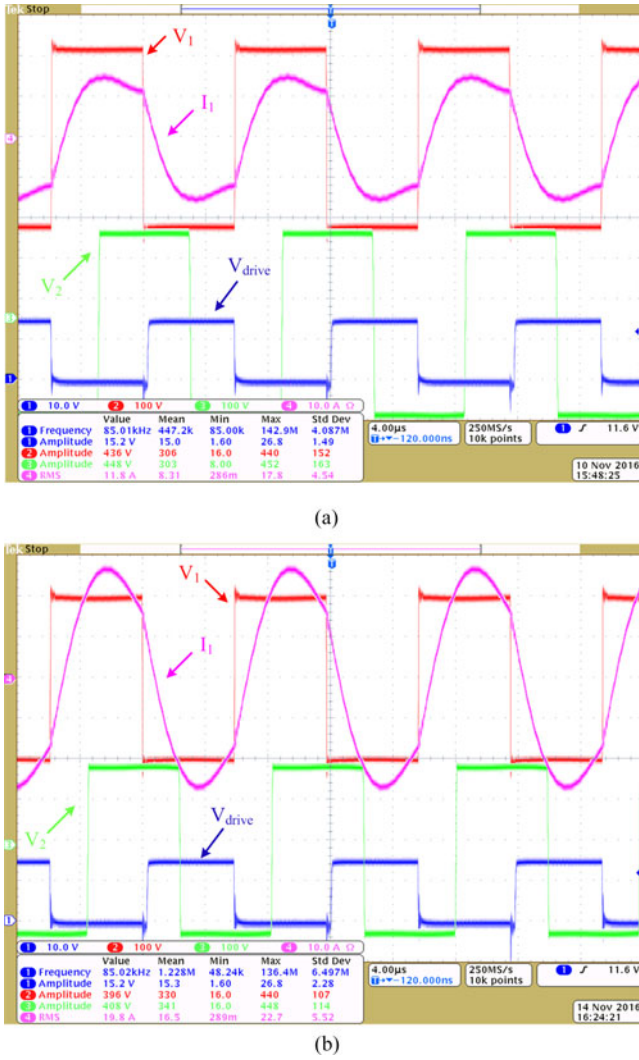Fig. 21. Experimental results of normalized power at different coupling coefficient k_{1-2} in the single- and dual-coupled systems.

The system is also tested in 150 mm x- and y-misalignment cases. The experimental waveforms are shown in Fig. 19.

The experimental waveforms show that soft switching can still be maintained in the misaligned cases, so the system can realize a relativly high efficiency. Fig. 19 also shows that there is no apparent noise in the drive signal V_{drive}.

With x- and y-misalignment, the output power is compared with the calculation in (18), as shown in Fig. 20. With 150 mm x-misalignment, the output power decreases to 1980 W, which is 56.8% of the well-aligned value. With -150 mm y-misalignment, it decreases to 2880 W (82.6% of the well-aligned value). With $+150$ mm y-misalignment, it is 3130 W (89.8% of the well-aligned value). It validates that the proposed system has good misalignment performance.

Fig. 20 also shows that experimental results are consistent with the calculation. Since the calculation is based on the FHA method and only the fundamental harmonic current is considered, the power difference in Fig. 20 can be explained by the presence of third-order har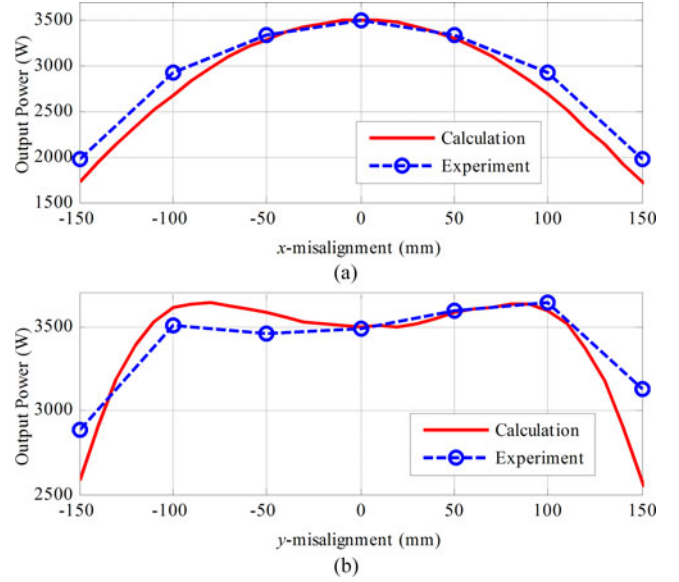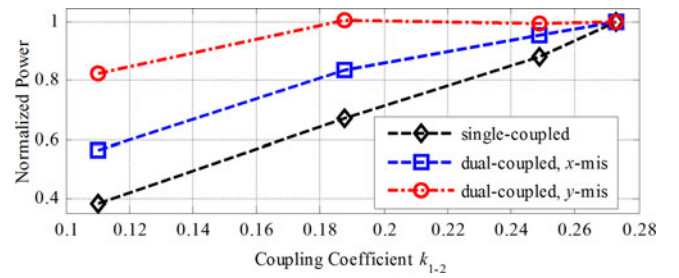monics [13]. Also, in Fig. 20(b), the output power is asymmetric. This is due to asymmetry in the DD structure of the hand-made inductors L_{f1} and L_{f2}.

The relationship between the normalized power and the main coupling coefficient k_{1-2} are also measured in the single- and dual-coupled systems as shown in Fig. 21.

In Fig. 21, the output power of the dual-coupled system are measured in both x- and y-misalignment cases. Compared to the single-coupled system, it indicates that the proposed system contributes to improve the misalignment performance, and the y-direction performance is improved even further.

VI. CONCLUSION AND FUTURE WORK

In this paper, a dual-coupled LCC-compensated IPT system is proposed to improve the misalignment performance. The compensation inductors are integrated into the main coils to transfer power to the secondary side. The circuit working principle of the dual-coupled IPT system is presented in detail, and it is shown that the magnetic couplings of the compensation inductors can improve the misalignment performance of an IPT system. Experimental results show that the proposed IPT system can retain at least 56.8% and 82.6% of the well-aligned power at 150 mm x- and y-direction misalignment, respectively.

In future research, a thorough economic analysis of the compensation inductors will be conducted to minimize the system cost, which includes short-term hardware cost and long-term energy cost during the life cycle. There is a tradeoff between the short- and long-term costs. For integrated inductors, since they share ferrite plates with the main coils, only the copper cost needs to be considered. If more copper is used, the short-term cost is increased but the long-term energy cost can be reduced due to higher efficiency.

REFERENCES

[1] R. Bosshard and J. W. Kolar, "Inductive power transfer for electric vehicle charging: Technical challenges and tradeoffs," *IEEE Power Electron. Mag.*, vol. 3, no. 3, pp. 22–30, Sep. 2016.

[2] G. Buja, M. Bertoluzzo, and K. N. Mude, "Design and experimentation of WPT charger for electric city car," *IEEE Trans. Ind. Electron.*, vol. 62, no. 12, pp. 7436–7447, Dec. 2015.

[3] F. Y. Lin, G. A. Covic, and J. T. Boys, "Evaluation of magnetic pad sizes and topologies for electric vehicle charging," *IEEE Trans. Power Electron.*, vol. 30, no. 11, pp. 6391–6407, Nov. 2015.

[4] J. Zhang, X. Yuan, C. Wang, and Y. He, "Comparative analysis of two-coil and three-coil structure for wireless power transfer," *IEEE Trans. Power Electron.*, vol. 32, no. 1, pp. 341–352, Jan. 2017.

[5] J. Deng, F. Lu, S. Li, T. D. Nguyen, and C. Mi, "Development of a high efficiency primary side controlled 7 kW wireless power charger," in *Proc. IEEE Int. Elect. Veh. Conf.*, 2014, pp. 1–6.

[6] Z. Zahid *et al.*, "Modeling and control of series-series compensated inductive power transfer system," *IEEE J. Emerg. Sel. Topics Power Electron.*, vol. 3, no. 1, pp. 111–123, Mar. 2015.

[7] W. Zhang, S. Wong, C. Tse, and Q. Chen, "Design for efficiency optimization and voltage controllability of series-series compensated inductive power transfer system, " *IEEE Trans. Power Electron.*, vol. 29, no. 1, pp. 191–200, Jan. 2014.

[8] J. Hou, Q. Chen, S. Wong, C. Tse, and X. Ruan, "Analysis and control of sereis/series-parallel compensated resonant converter for contactless power transfer," *IEEE J. Emerg. Sel. Topics Power Electron.*, vol. 3, no. 1, pp. 124–136, Mar. 2015.

[9] Y. H. Sohn, B. H. Choi, E. S. Lee, G. C. Lim, G. Cho, and C. T. Rim, "General unified analysis of two-capacitor inductive power transfer systems: Equivalence of current-source SS and SP compensations," *IEEE Trans. Power Electron.*, vol. 30, no. 11, pp. 6030–6045, Nov. 2015.

[10] W. Zhang, S. Wong, C. Tse, and Q. Chen, "Analysis and comparison of secondary series- and parallel-compensated inductive power transfer systems operating for optimal efficiency and load-independent voltage-transfer ratio," *IEEE Trans. Power Electron.*, vol. 29, no. 6, pp. 2979–2990, Jun. 2014.

[11] H. Feng, T. Cai, S. Duan, J. Zhao, X. Zhang, and C. Cheng, "An LCC-compensated resonant converter optimized for robust reaction to large coupling variation in dynamic wireless power transfer," *IEEE Trans. Ind. Electron.*, vol. 63, no. 10, pp. 6591–6601, Oct. 2016.

[12] C. Liu, S. Ge, Y. Guo, H. Li, and G. Cai, "Double-LCL resonant compensation network for electric vehicles wireless power transfer: Experimental study and analysis," *IET Power Electron.*, vol. 9, no. 11, pp. 2262–2270, 2016.

[13] S. Li, W. Li, J. Deng, T. D. Nguyen, and C. Mi, "A double-sided LCC compensation network and its tuning method for wireless power transfer," *IEEE Trans. Veh. Technol.*, vol. 64, no. 6, pp. 2261–2273, Jun. 2015.

[14] F. Lu, H. Zhang, H. Hofmann, and C. Mi, "A dynamic charging system with reduced output power pulsation for electric vehicles," *IEEE Trans. Ind. Electron.*, vol. 63, no. 10, pp. 6580–6590, Oct. 2016.

[15] W. Zhang and C. Mi, "Compensation topologies of high-power wireless power transfer systems," *IEEE Trans. Veh. Technol.*, vol. 65, no. 6, pp. 4768–4778, Jun. 2016.

[16] W. Li, H. Zhao, J. Deng, T. Kan, and C. Mi, "Integrated LCC compensation topology for wireless charger in electric and plug-in electric vehicles," *IEEE Trans. Ind. Electron.*, vol. 62, no. 7, pp. 4215–4225, Jul. 2015.

[17] F. Lu, H. Zhang, H. Hofmann, and C. Mi, "A high efficiency 3.3 kW loosely-coupled wireless power transfer system without magnetic material," in *Proc. IEEE Energy Conv. Cong. Expo.*, 2015, pp. 2282–2286.

[18] J. Deng, W. Li, T. D. Nguyen, S. Li, and C. Mi, "Compact and efficient bipolar coupler for wireless power chargers: Design and analysis," *IEEE Trans. Power Electron.*, vol. 30, no. 11, pp. 6130–6140, Nov. 2015.

[19] F. Lu *et al.*, "A high efficiency and compact inductive power transfer system compatible with both 3.3 kW and 7.7 kW receivers," in *Proc. IEEE Appl. Power Electron. Conf. Expo.*, 2017, pp. 3669–3673.

[20] T. Kan, T. D. Nguyen, J. C. White, R. K. Malhan, and C. Mi, "A new integration method for an electric vehicle wireless charging system using LCC compensation topology: Analysis and design," *IEEE Trans. Power Electron.*, vol. 32, no. 2, pp. 1638–1650, Feb. 2017.

[21] J. Deng, W. Li, S. Li, and C. Mi, "Magnetic integration of LCC compensated resonant converter for inductive power transfer applications," in *Proc. IEEE Energy Conv. Cong. Expo.*, 2014, pp. 660–667.

[22] R. Bosshard, U. Iruretagoyena, and J. W. Kolar, "Comprehensive evaluation of rectangular and double-D coil geometry for 50 kW/85 kHz IPT system," *IEEE J. Emerg. Sel. Top. Power Electron.*, vol. 4, no. 4, pp. 1406–1415, 2016.

[23] M. Budhia, J. T. Boys, G. A. Covic, and C. Y. Huang, "Development of a single-sided flux magnetic coupler for electric vehicle IPT charging systems," *IEEE Trans. Ind. Electron.*, vol. 60, no. 1, pp. 318–328, Jan. 2013.

[24] S. Y. Choi, S. Y. Jeong, E. S. Lee, B. W. Gu, S. W. Lee, and C. T. Rim, "Generalized models on self-decoupled dual pick-up coils for large lateral tolerance," *IEEE Trans. Power Electron.*, vol. 30, no. 11, pp. 6434–6445, Nov. 2015.

[25] G. R. Nagendra, J. T. Boys, G. A. Covic, B. S. Riar, and A. Sondhi, "Design of a double coupled IPT EV highway," in *Proc. IEEE Ind. Electron. Conf.*, 2013, pp. 4606–4611.

[26] S. Zhou and C. Mi, "Multi-paralleled LCC reactive power compensation networks and their tuning method for electric vehicle dynamic wireless charging," *IEEE Trans. Ind. Electron.*, vol. 63, no. 10, pp. 6546–6556, Oct. 2016.

[27] F. Lu, H. Zhang, H. Hofmann, and C. Mi, "A dual-coupled LCC-compensated IPT system to improve misalignment performance," in *Proc. IEEE Wireless Power Transfer Workshop*, 2017, pp. 1–8.

[28] R. Bosshard and J. W. Kolar, "Multi-objective optimization of 50 kW/85 kHz IPT system for public transport," *IEEE J. Emerg. Sel. Top. Power Electron.*, vol. 4, no. 4, pp. 1370–1382, Dec. 2016.

[29] SAE Wireless Power Transfer for Light-Duty Plug-In and Electric Vehicles and Alignment Methodology, SAE Standard J2954, May 2016.

[30] ICNIRP "Guidelines for limiting exposure to time-varying electric, magnetic and electromagnetic fields (1 Hz to 100 kHz)," *Health Phys.*, vol. 99, pp. 818–836, 2010.

[31] Z. Bi, T. Kan, C. Mi, Y. Zhang, Z. Zhao, and G. Keoleian, "A review of wireless power transfer for electric vehicles: Prospects to enhance sustainable mobility," *Appl. Energy*, vol. 179, pp. 413–425, 2016.
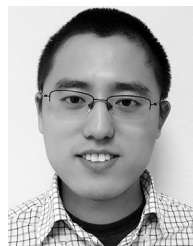
Fei Lu (S'12) received the B.S. and M.S. degrees from the Harbin Institute of Technology, Harbin, China, in 2010 and 2012, respectively, and the Ph.D. degree from the University of Michigan, Ann Arbor, MI, USA, in 2017, all in electrical engineering.

He is currently a Postdoc Researcher in San Diego State University, San Diego, CA, USA. His research topic focuses on wireless power transfer for the application of electric vehicle charging. He is working on the high power and high efficiency capacitive power transfer through an air-gap distance up to 100's of millimeters. He is also working on the application of wide bandgap devices on WPT system.

Hua Zhang (S'14) received the B.S. and M.S. degrees in electrical engineering from Northwestern Polytechnical University, Xi'an, China, in 2011 and 2014, respectively. She is currently working toward the Ph.D. degree in electrical engineering from the Northwestern Polytechnical University, Xi'an, China.

From September 2014 to August 2015, she was a joint Ph.D. student founded by the China Scholarship Council with the University of Michigan, Dearborn, MI, USA. From September 2015, she started to work in San Diego State University, San Diego, CA, USA. Her research is about the coupler design of high-power IPT and CPT system.

Heath Hofmann (M'89–SM'15) received the B.S. degree in electrical engineering from The University of Texas at Austin, Austin, TX, USA, in 1992, and the M.S. and Ph.D. degrees in electrical engineering and computer science from the University of California, Berkeley, CA, USA, in 1997 and 1998, respectively.

He is currently an Associate Professor with the University of Michigan, Ann Arbor, Michigan, USA. His research interests include the design, analysis, and control of electromechanical systems, and power electronics.

Wencong Su (S'06–M'13) received the B.S. degree (with distinction) from Clarkson University, Potsdam, NY, USA, in 2008, the M.S. degree from Virginia Polytechnic Institute and State University, Blacksburg, VA, USA, in 2009, and the Ph.D. degree from North Carolina State University, Raleigh, NC, USA, in 2013, all in electrical engineering.

He is currently an Assistant Professor in the Department of Electrical and Computer Engineering, University of Michigan, Dearborn, MI, USA. His research interests include power and energy systems, electrified transportation systems, cyber physical systems, and electricity markets.

Chunting Chris Mi (S'00–A'01–M'01–SM'03–F'12) received the B.S.E.E. and M.S.E.E. degrees in electrical engineering from Northwestern Polytechnical University, Xi'an, China, and the Ph.D. degree in electrical engineering from the University of Toronto, Toronto, ON, Canada, in 1985, 1988, and 2001, respectively.

He is a Professor and the Chair of electrical and computer engineering and the Director of the Department of Energy-funded Graduate Automotive Technology Education (GATE) Center for Electric Drive Transportation, San Diego State University (SDSU), San Diego, CA, USA. Prior to joining SDSU, he was with with University of Michigan, Dearborn, MI, USA, from 2001 to 2015. He was the President and the Chief Technical Officer of 1Power Solutions, Inc., from 2008 to 2011. He is the Cofounder of Gannon Motors and Controls LLC and Mia Motors, Inc. His research interests include electric drives, power electronics, electric machines, renewable-energy systems, and electrical and hybrid vehicles. He has conducted extensive research and has published more than 100 journal papers. He has taught tutorials and seminars on the subject of HEVs/PHEVs for the Society of Automotive Engineers (SAE), the IEEE, workshops sponsored by the National Science Foundation, and the National Society of Professional Engineers. He has delivered courses to major automotive OEMs and suppliers, including GM, Ford, Chrysler, Honda, Hyundai, Tyco Electronics, A&D Technology, Johnson Controls, Quantum Technology, Delphi, and the European Ph.D School. He has offered tutorials in many countries, including the U.S., China, Korea, Singapore, Italy, France, and Mexico. He has published more than 100 articles and delivered 30 invited talks and keynote speeches.

Dr. Mi has also served as a Panelist in major IEEE and SAE conferences.